Scripta Materialia 242 (2024) 115946

Contents lists available at ScienceDirect

Scripta Materialia

journal homepage: www.journals.elsevier.com/scripta-materialia

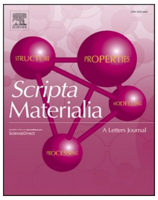

In situ synchrotron X-ray diffraction analysis of ultrasonically assisted microstructure refinement during laser melting process

Tianzhao Wang [a], Benjamin Schneiderman [b], Samuel J. Clark [c], Andrew Chihpin Chuang [c,*], Zhenzhen Yu [b,*], Xun Liu [a,*]

[a] *Welding Engineering, Department of Materials Science and Engineering, The Ohio State University, 1248 Arthur E Adams Dr, Columbus, OH 43221, USA*
[b] *George S. Ansell Department of Metallurgical and Materials Engineering, Colorado School of Mines, 1500 Illinois St, Golden, CO 80401, USA*
[c] *Advanced Photon Source, Argonne National Laboratory, 9700 S. Cass Ave, Lemont, IL 60439, USA*

ARTICLE INFO

Keywords:
In situ synchrotron x-ray diffraction
Electron backscatter diffraction
Ultrasonic Treatment
Laser melting

ABSTRACT

This work investigates the effect of ultrasonic treatment (UST) on the microstructure of AA4043 alloy during laser melting process. The study utilizes in situ synchrotron X-ray diffraction (SXRD) and postmortem electron backscatter diffraction (EBSD) techniques to examine the ultrasonic grain refinement mechanism. The SXRD diffraction patterns exhibit higher continuity of major diffraction rings in the UST-test pattern, indicating a more refined grain structure. The presence of new diffraction spots in the post-test diffraction pattern with UST suggests the breakdown of epitaxial growth of columnar dendrites during solidification. Thermal profiles determined by analyzing the lattice parameter evolution show a faster cooling rate with UST. The inverse pole figures and aspect ratio distribution from EBSD reveal that the UST samples exhibit a refined, more equiaxed grain structure along the weld centerline. UST sample also develops more fine-sized low angle grain boundaries (LAGBs). These features offer better hot-cracking resistance in aluminum alloys.

The growing application of ultrasound in molten metal processes is attributed to its capacity for grain refinement, primarily through the ultrasonic-induced acoustic cavitation and streaming [1]. Acoustic cavitation generates alternating positive and negative pressure field in the melt which drives pulsation of cavitation bubbles in tandem with oscillation. Upon the positive pressure phases, the gas bubbles tend to collapse implosively, releasing energy into the surrounding melt. Such implosion generates high pressure up to 1 GPa and cumulative jets with velocities up to 100 m/s [2]. The acoustic streaming effect describes steady state flows that are driven by ultrasound, acting over longer spatial distances but with a lower flow velocity of a few m/s [3]. The jets upon bubble collapse initiate dendrite fragmentations, which are further dispersed in the melt by the long-range acoustic streaming and act as nucleation sites [4]. The high-pressure field resulting from bubble collapse elevates the melting point, which increases local undercooling and promotes nucleation over grain growth [5]. Furthermore, ultrasound enhances heterogeneous nucleation by improving the wettability of nonmetal inclusion particles [6]. These mechanisms of ultrasonic refinement have been studied via in situ synchrotron X-ray radiography [7–10], showing that both acoustic cavitation and streaming contributed to the dendrite fragmentation. A recent study utilized ultra-fast X-ray tomography technique to examine the UST in 3D and revealed that acoustic flow induced dendrite fragmentation via both dendrite remelting and mechanical fracture, resulting in 20~25 % of grain refinement within 10 s [11]. High-speed in situ imaging of growing dendrites subjected to a 50 W UST revealed that the cyclic pressure could lead to fatigue fracture of growing dendrites within 50 ms [12].

The information obtained through the in situ synchrotron X-ray radiography studies of UST is limited to fluid flows. In comparison, in situ synchrotron X-ray diffraction (SXRD) can provide more complete understanding of the process including texture, thermal history, and phase evolution [13]. So far, SXRD of UST process has not been performed in literature and holds significant potential as a new monitoring technique for advanced analysis for UST-assisted processes.

The factors that influence the UST effect on microstructure refinement include amplitude, inoculation, melt composition, and processing time [1,2,14,15]. Compared with conventional casting process, additive manufacturing (AM) is associated with high cooling and solidification rate, making the application of UST more complicated with AM processes. In previous synchrotron imaging analysis of the ultrasound

---

* Corresponding author.
E-mail addresses: cchuang@anl.gov (A.C. Chuang), zyu@mines.edu (Z. Yu), liu.7054@osu.edu (X. Liu).

https://doi.org/10.1016/j.scriptamat.2023.115946
Received 6 October 2023; Received in revised form 12 December 2023; Accepted 17 December 2023

treated casting process [16], the cooling rate was around 1.5 °C/s. In comparison, in laser-based AM processes, the cooling rate reaches up to 1000 °C/s [17]. In this work, we integrated an ultrasonic system to the existing laser-based AM replicator [18,19] at Argonne National Laboratory Advanced Photon Source (APS) beamline 1-ID-E, USA to investigate the ultrasonic effect in a laser melting process.

Fig. 1(a) illustrates the ultrasound-assisted AM replicator at APS. The ultrasonic horn was threaded in with a commercial AA4043 aluminum rod with a diameter of 2.54 mm (AlcoTec 4043 5 %Si) and a hockey stick geometry. The end section of the rod was machined into a 1 mm thin sheet, placed perpendicular to, and located beneath the laser. The specimen was vibrating at 40 kHz along the longitudinal axis of the rod-shape part of the sample during the SXRD test. The assembled setup was shown in Fig. 1(b). The vibration amplitude at the sample end was measured as 6 μm via laser vibrometer, corresponding to an ultrasonic intensity of 350 W/cm^2 [20], which exceeded the reported threshold intensity for acoustic cavitation in pure molten aluminum [15]. A monochromatic X-ray beam with an energy of 61.33 keV was directed through the specimen. A laser source scanned transversely across the sample thickness at a speed of 0.1 m/s with a spot diameter of 120 μm at the top edge of the specimen. The laser power was set to 400 W, to generate a fully melted condition throughout the specimen thickness direction, allowing the complete solidification process to be analyzed. The X-ray radiography images were captured by a Point Grey (GS3-U3–23S6M) camera through a 25 μm LuAG:Ce scintillator. The radiography imaging field of view was 2.25 mm × 1.40 mm and the X-ray diffraction beam size was 50 μm × 30 μm, with the beam positioned 20 μm below the sample top surface. The diffraction patterns were captured with a PILATUS3X-2 M CdTe X-ray detector (DECTRIS, Switzerland) at a frame rate of 250 Hz and an exposure time of 1 ms per frame. The ultrasonic vibration was initiated before the start of laser beam scanning and turned off 1 s after the process ended.

Fig. 1(c) and (d) show the radiography images captured before and after the tests. The red box marks the X-ray beam location during the in situ SXRD test. The beam center is located near the melt centerline. Additionally, static diffraction patterns were collected before and after the SXRD test at the same location using a longer exposure time of 100 ms.

To quantitatively evaluate the continuity of the Debye-Scherrer rings, the 2D static diffraction patterns were converted to 16-bit gray-scale images. The circumferential profiles of the first three diffraction rings were extracted azimuthally using the ImageJ software. The continuity was determined by measuring the length of the perimeter containing bright diffraction spots and dividing it by the total ring perimeter. This was achieved by applying a threshold grayscale value of 5 to the background level.

To obtain the thermal history during the in situ SXRD test, the 2D diffraction patterns from each detector frame were integrated into 1D spectra using the open source Fit2D software. The diffraction peak centers were determined by fitting the profile with a Pseudo-Voigt function. Lattice parameters a_{hkl} were subsequently calculated based on Bragg's law for FCC crystal structure based upon major peaks,

$$a_{hkl} = \frac{\lambda\sqrt{h^2+k^2+l^2}}{2\sin\theta_{hkl}}$$

where λ is the X-ray wavelength, θ_{hkl} is the diffraction angle and $h, k,$ and l are the Miller indices of the lattice plane. Together with the temperature-dependent coefficient of thermal expansion (CTE) determined from the JMatPro software, the temperature profiles were calculated via a recursion equation [13], applied starting when the sample was cooled to room temperature and moving backward in time:

$$T_{i-1} = T_i + \frac{a_{i-1} - a_i}{CTE_i * a_i}$$

where T_i represents the temperature, a_i corresponds to the average lat-

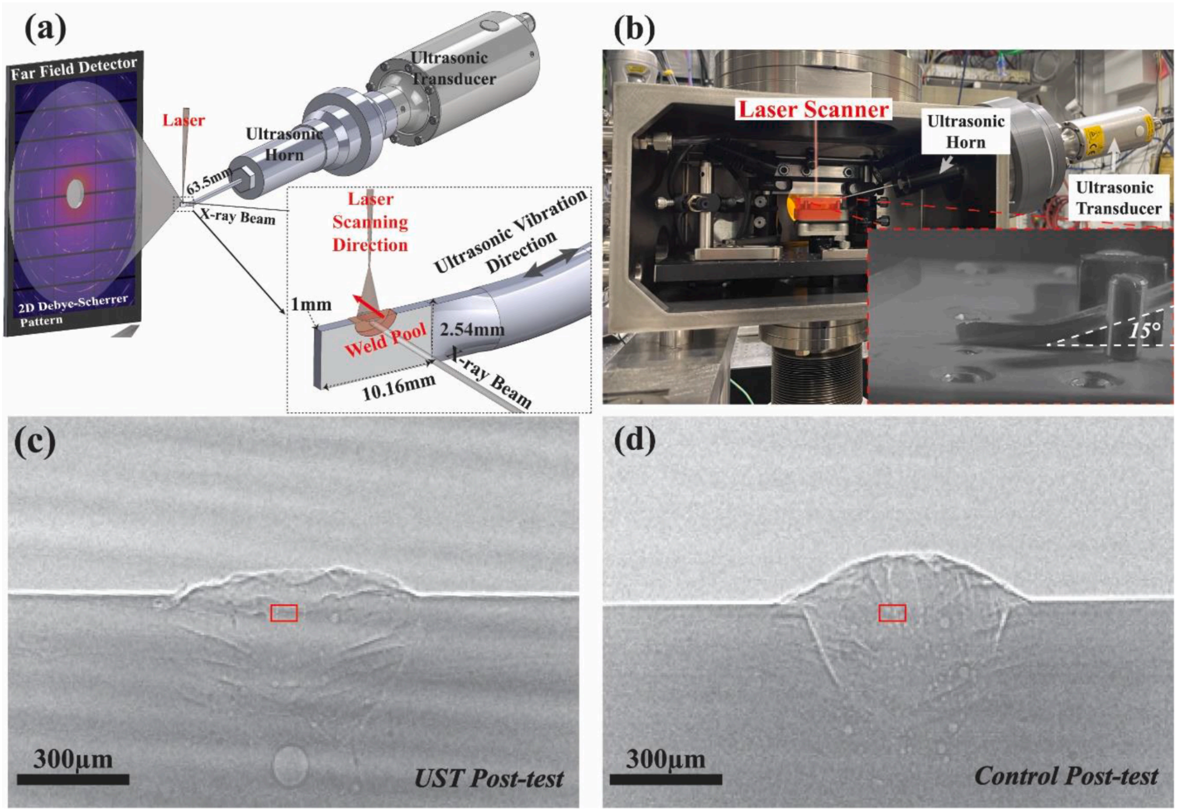

Fig. 1. (a) schematic of in situ synchrotron X-ray diffraction test and imaging experiment, (b) photo of the assembled UST-SXRD setup, and post-melting radiography images with (c) UST and (d) control test without UST. The red box represents the x-ray beam size and location of diffraction measurement.

tice parameter, and CTE_i is the temperature dependent coefficient of thermal expansion at time frame *i*. The lattice parameters can also be affected by elastic strain. However, a stress of 70 MPa (Yield Stress of AA4043) only leads to an elastic strain of 0.0009 at room temperature based on Young's modulus computed by JMatPro, whereas an increase of 100 °C in temperature results in a lattice distortion of 0.004. Thus, the temperature induced lattice expansion holds a more dominant role during the cooling stage after solidification [18].

Samples for electron backscatter diffraction (EBSD) analysis were prepared following the standard metallographic procedure. The polished samples were etched by Keller's reagent and observed with optical microscopy. Quantitative dendrite analysis was performed using the Mipar software.

As shown in Fig. 2(a) and (b), both the UST and control samples exhibit similar melt penetration depth. The melt width is larger in the UST sample, measuring 625 μm, compared to 595 μm in the control sample. The total height of the UST weld is 501 μm, which is lower than the control weld height of 541 μm. The geometries observed at this specific cross-section aligned with the radiography images in Fig. 1(a) and (d), which represent two-dimensional projections of the sample along the transverse direction. The wider weld pool with a flatter surface from UST could be contributed by the enhanced melt flow through acoustic streaming. Additionally, the centerline regions in two cases show different dendritic structures. Aspect ratio describes the morphology of grains, which is defined as the quotient between the longest and shortest axis. A larger aspect ratio indicates elongated columnar grains while a smaller value corresponds to more equiaxed grains. Based on the microstructure at this particular cross-section, coarse columnar dendrite structures with large aspect ratios are observed along the control weld centerline, while the UST weld centerline exhibits more refined low-aspect-ratio dendrites on the cross section examined, as shown in Fig. 2(c) and (d).

Fig. 3 depicts the static diffraction patterns captured before and after the laser melting test in the UST and control samples. The continuity of the rings correlates with the number of grains within the X-ray beam pathway. A larger number of grains, i.e., refined grain structure for the same X-ray beam size, corresponds to diffractions occurring along various directions and accordingly more continuous diffraction rings. The continuity of the rings decreased after the laser melting and solidification in both the UST and control conditions. However, after melting with UST, new diffraction spots emerged in the (200) and (220) rings, in regions where no spots were present prior to melting. These newly formed spots are marked by white boxes in Fig. 3(a1) and (a2). The circumferential profiles of diffraction rings over azimuthal angles provide a more direct comparison. In Fig. 3(c1), new spots are visible in the (200) and (220) spectra when UST is applied, as indicted by black boxes. In the control sample, most of the post-test diffraction spots can be traced back to the pre-test spots, as shown in Fig. 3(c2). The formations of new diffraction spots were more clearly observed in the in situ diffraction pattern evolution, as provided in the supplementary data.

Table 1 shows the calculated continuities of all conditions. The UST sample exhibits slight diminution of ring continuities, whereas the control sample shows a significant decrease in all (111), (200), and (220) rings. The UST case shows minor reductions of 3 %, 2 %, and 3 % in the three rings, whereas the control sample demonstrates substantial decreases of 20 %, 14 %, and 20 % in the corresponding rings. As discussed in the introduction, the UST-induced grain refinement effect relies on dendrite fragmentation and enhanced heterogeneous nucleation [3]. Both effects interrupt ongoing epitaxial growth, and promote nucleation, which aligns with the formation of new spots and the higher ring continuity with UST sample.

To further characterize the UST effect, EBSD analysis was carried out on the transverse cross section of laser remelted samples, as shown in Fig. 4. The inverse pole figures (IPF) are compared in Fig. 4(a1) and (a2). Large elongated columnar grain structures dominate in the control sample, especially along the centerline, whereas the UST sample shows a

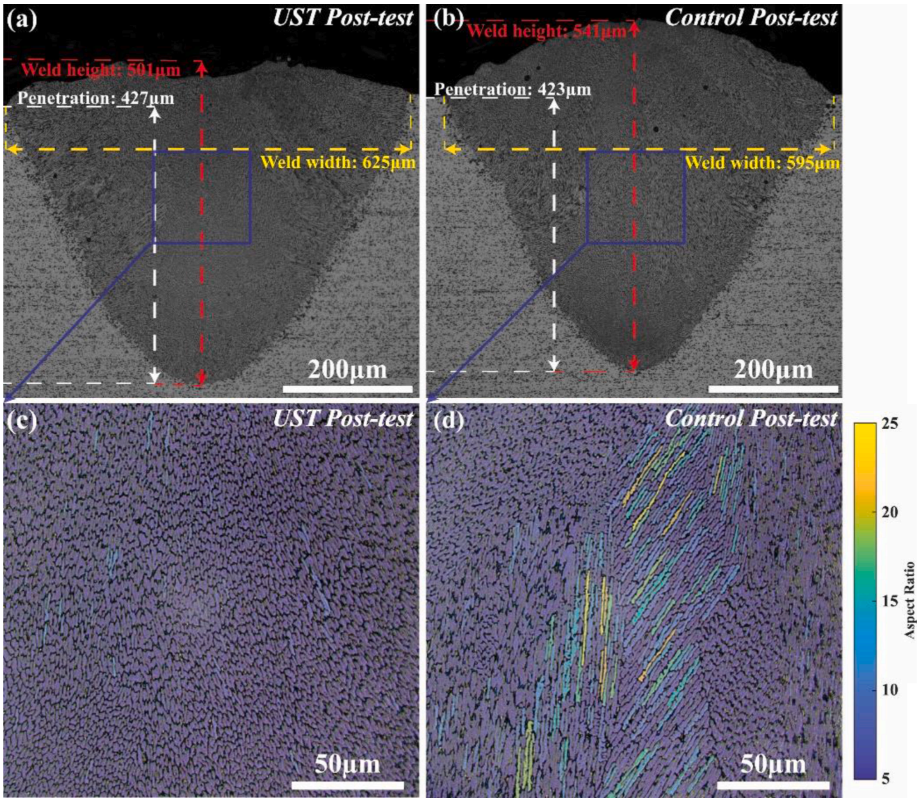

Fig. 2. Optical macrographs showing the post-test weld cross-section in the case of (a) UST and (b) control sample; Aspect ratio analysis along the centerline of (c) UST sample and (d) control sample.

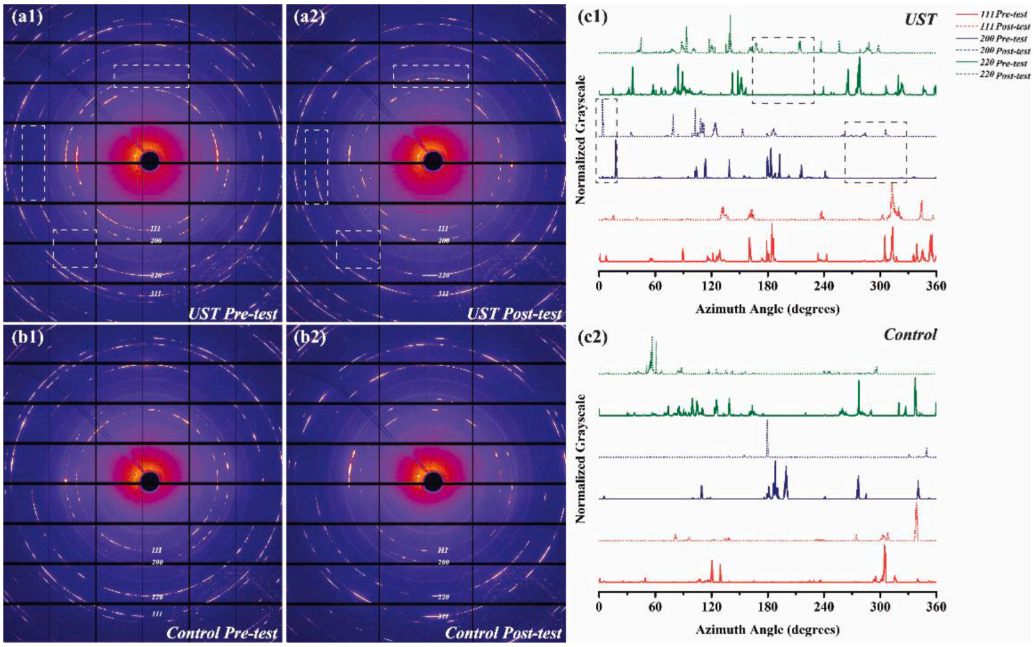

Fig. 3. Static diffraction patterns with UST (a1) before and (a2) after the laser melting test; Static diffraction patterns of the control sample (b1) before and (b2) after the laser melting test; Circumferential profiles of major diffraction rings extracted from static diffraction patterns with (c1) UST and (c2) control sample.

Table 1
Continuity of 111, 200, and 220 rings before and after the laser melting test.

	111 Ring	200 Ring	220 Ring
UST Pre-test	40 %	27 %	30 %
UST Post-test	37 %	25 %	27 %
Continuity Decrease	**3 %**	**2 %**	**3 %**
Control Pre-test	39 %	23 %	33 %
Control Post-test	19 %	9 %	13 %
Continuity Decrease	**20 %**	**14 %**	**20 %**

more refined morphology. Considering the thermal histories at different locations in the melt during the solidification process, the centerline experienced longer fusion duration, which allows longer ultrasound-melt interaction time and exhibits the most significant refining effect.

Fig. 4(b1) and (b2) present the grain boundary distribution for the UST and control sample, respectively. Grain boundaries were categorized into low angle grain boundaries (LAGBs) and high angle grain boundaries (HAGBs) by a threshold boundary misorientation of 15° (except for Coincidence Site Lattice). More fine grains with LAGBs were observed in the centerline region of UST sample, while coarse grains with HAGBs were mostly observed in the control sample.

LAGBs were found to be less susceptible to hot-cracking than HAGBs [21,22] due to the difference in grain boundary energies (γ_{gb}). The γ_{gb} at LAGBs are smaller than the solid-liquid interface energy at both grains, which is twice of the γ_{sl}, leaving the liquid film at LAGB unstable and thus preventing liquation of the boundary. In HAGBs, the γ_{gb} exceeds twice the γ_{sl} and allows stable liquid film at the grain boundaries. This study indicates UST promotes the development of LAGBs and accordingly improves hot-cracking resistance. The observed LAGBs increase by UST corroborates previous studies of UST-assisted AM processes [23, 24]. Fig. 4(c1) and (c2) compare the grain aspect ratio reciprocal (width/length) distribution in UST and control samples. In this case, an aspect ratio reciprocal closer to 1 corresponds to a more equiaxed grain morphology. The centerline regions in the UST sample yield a higher aspect ratio reciprocal than the control one. This observation is in accordance with previous studies on UST assisted laser-based AM and welding processes [24,25], which is contributed by dendrite fragmentation and enhanced undercooling [2].

Grain orientation spread (GOS) maps are shown in Fig. 4(d). GOS corresponds to the misorientation distribution within an individual grain by calculating the average misorientation angle between the orientation of all pixels and the mean orientation of the grain [26]. The UST sample shows higher GOS values in the grains along the centerline, indicating a broader range of orientations of the dendrites within individual grains, which could be attributed to UST-induced dendrite fragmentation during the terminal stage of solidification.

The thermal histories determined based on the evolution of lattice parameters (plotted in Fig. 5(a) and (b)) are shown in Fig. 5(c). The cooling rates are extracted by taking the first order derivative of the temperature profiles, see Fig. 5(d). Higher cooling rates are observed in the UST process, which also contributes to microstructure refinement [27].

The impact of ultrasonic treatment on the cooling rate during the solidification process has been measured by thermocouples. Multiple studies have reported that ultrasonic treatment increases the cooling rate [1,3,28,29]. However, the ultrasonic effect in conventional UST setups is convoluted by the heat dissipation from the ultrasonic horn. Even though the ultrasonic horn was preheated prior to the temperature measurements [28], it could still serve as a heat dissipating path. The cooling rates obtained in current work eliminate this temperature measurement artifact, since the thermal boundary conditions are identical in UST and control sample with the same experimental setup. Heat generated during the test, both from the laser system and ultrasound, followed the same dissipation paths of conduction via the sample itself, convection on the top surface, and radiation to the surrounding environment. Furthermore, the temperature profiles were calculated directly from the lattice parameters, eliminating the uncertainties from thermocouple probing method with the delayed response time and the additional heat dissipation via thermocouple probe. The increased cooling rate can be attributed to the UST-activated convection melt flow caused by the acoustic cavitation and streaming, which therefore enhanced the latent heat dissipation [30]. However, the factors that influence cooling rate can be more complicated. Ultrasonic power, ultrasonic energy implementation method, and melt materials could all impact the solidification behavior during UST. Further comprehensive analysis is required to obtain a more thorough understanding.

This work analyzed the microstructure refinement effect of UST in a

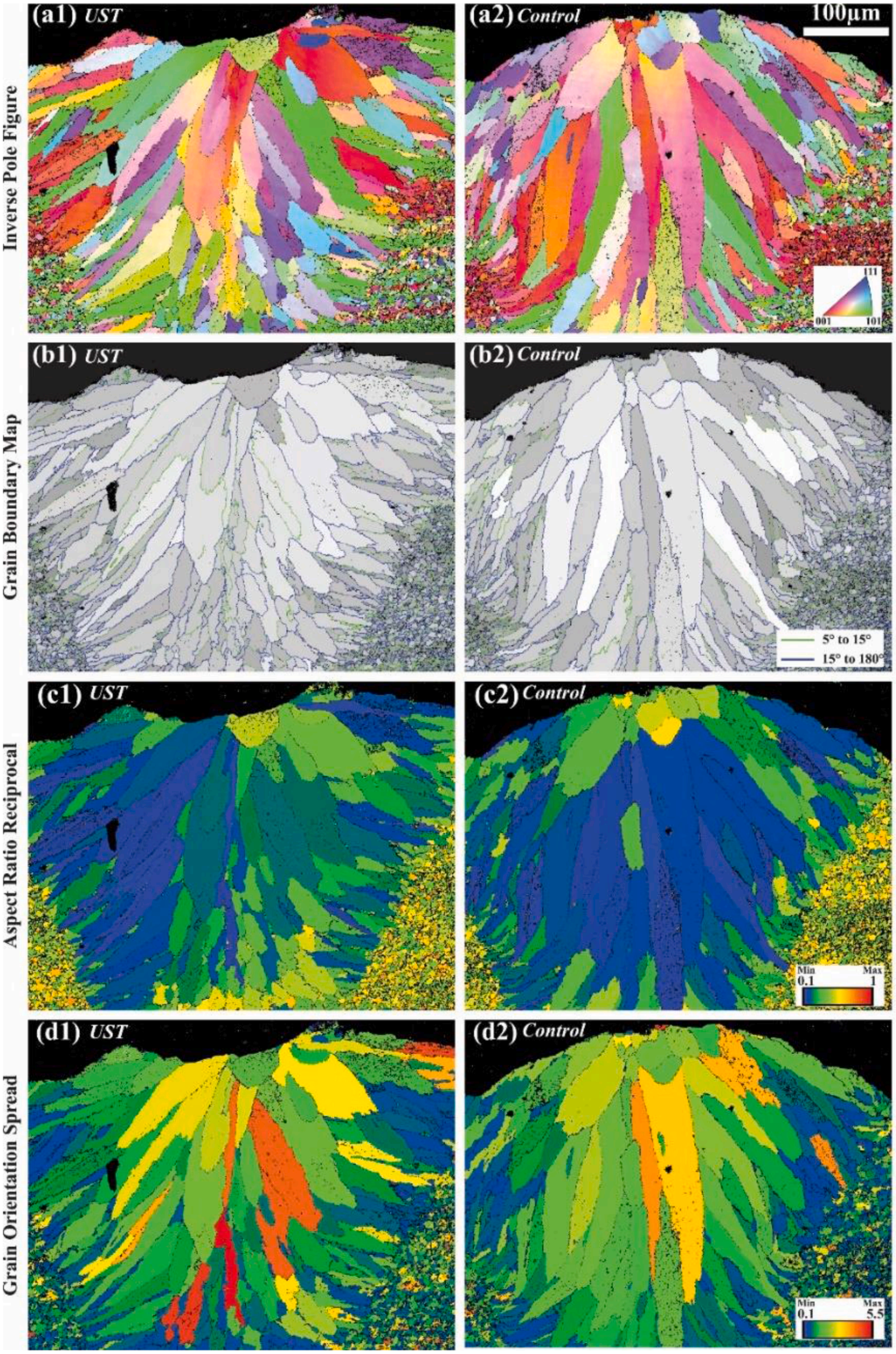

Fig. 4. EBSD analysis of laser remelted samples: inverse pole figure of (a1) UST and (a2) control samples; Grain boundary distribution of (b1) UST and (b2) control samples; Aspect ratio reciprocal distribution of (c1) UST and (c2) control samples; Grain orientation spread of (d1) UST and (d2) control sample.

laser AM environment, which is replicated by an ultrasonically assisted laser melting system. Static diffraction patterns reveal that UST samples yield higher continuity of diffraction rings, corresponding to a more refined grain structure. Besides, new diffraction spots appeared in the post-UST pattern, indicating promoted heterogeneous nucleation of new grains over epitaxial grain growth, which was further validated by the in situ SXRD analysis. Thermal histories derived from lattice parameters measurement based on the in situ diffraction profiles demonstrated higher cooling rates under UST. Post-mortem EBSD analysis showed a more refined grain structure, more LAGBs, and higher GOS along the UST sample centerline. These findings imply that laser-based AM processes of aluminum alloys can benefit from the incorporation of UST,

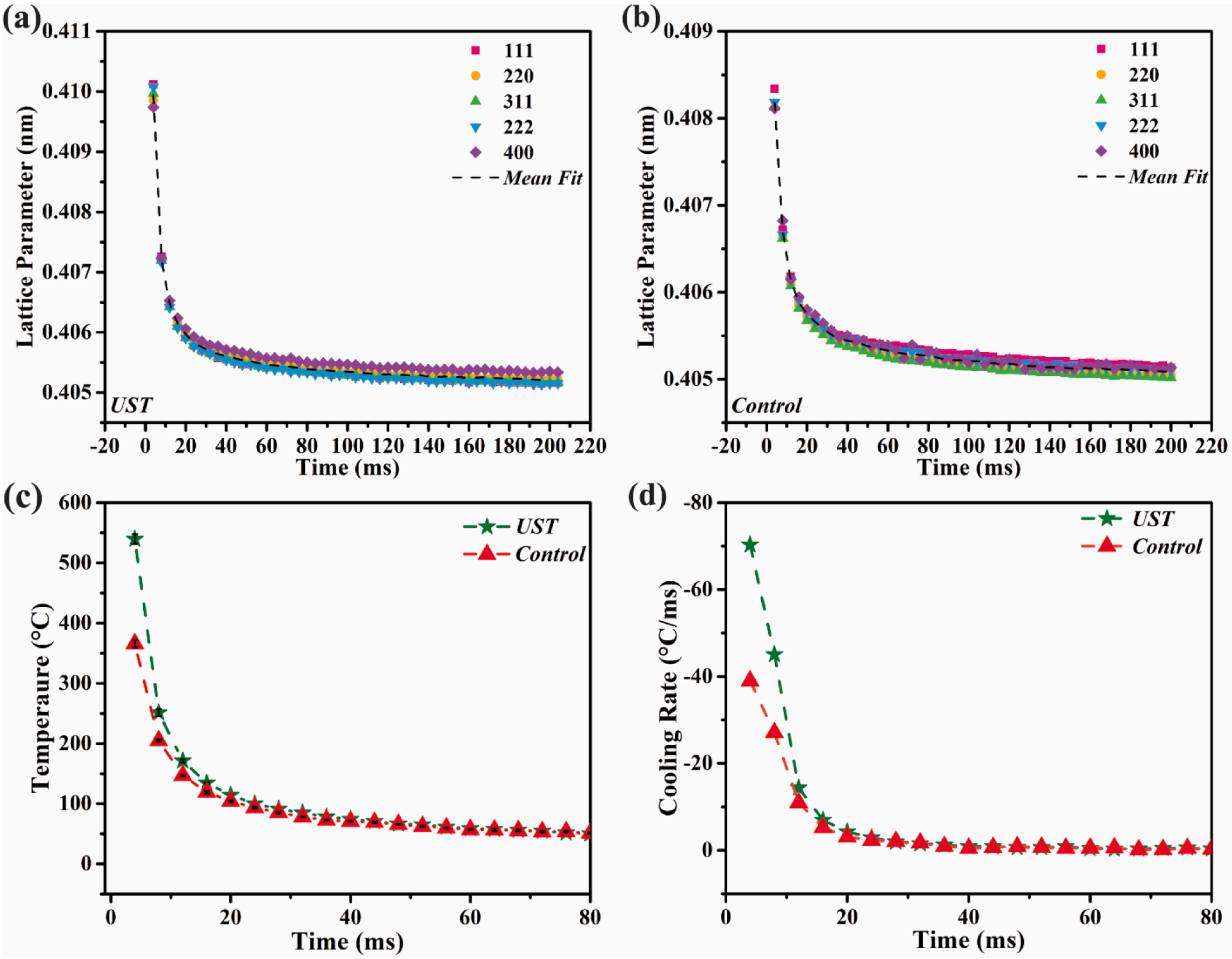

Fig. 5. Lattice parameters calculated based on peak centers with (a) UST and (b) control sample; (c) Temperature profiles with error bars in black color and (d) cooling rates based on average lattice parameters.

resulting in a refined microstructure and reduced susceptibility to hot cracking.

Declaration of Competing Interest

We hereby declare that the work is based on our original work, has not been published before and is not currently being considered for publication elsewhere. We know of no conflicts of interest associated with this submission, and there has been no significant financial support for this work that could have influenced the conclusions. We confirm that this work has been read and approved for submission by all listed authors.

Acknowledgement

This work is supported by National Science Foundation, CMMI AM Award # 2044526: CAREER: Ultrasonically Assisted Wire Arc Additive Manufacturing of Metal Matrix Nanocomposites for High-strength, Lightweight Structures, and Award # 1847630. This research used resources of the Advanced Photon Source, a U.S. Department of Energy (DOE) Office of Science User Facility operated for the DOE Office of Science by Argonne National Laboratory under Contract No. DE-AC02-06CH11357. Data was collected at Beamline 1-ID-E. Support from beamline staff was greatly appreciated. Electron microscopy was performed at the Center for Electron Microscopy and Analysis (CEMAS) at The Ohio State University.

Supplementary materials

Supplementary material associated with this article can be found, in the online version, at doi:10.1016/j.scriptamat.2023.115946.

References

[1] H.R. Kotadia, M. Qian, D.G. Eskin, A. Das, On the microstructural refinement in commercial purity Al and Al-10 wt% Cu alloy under ultrasonication during solidification, Mater. Des. 132 (2017) 266–274, https://doi.org/10.1016/j.matdes.2017.06.065.

[2] G.I. Eskin, Broad prospects for commercial application of the ultrasonic (cavitation) melt treatment of light alloys, Ultrason. Sonochem. 8 (2001) 319–325, https://doi.org/10.1016/S1350-4177(00)00074-2.

[3] H.R. Kotadia, M. Qian, A. Das, Solidification of aluminium alloys under ultrasonication: an overview, Trans. Ind. Inst. Met. 71 (2018) 2681–2686, https://doi.org/10.1007/s12666-018-1446-1.

[4] G.I. Eskin, D.G. Eskin, Ultrasonic Grain Refinement, in: Ultrasonic treatment of light alloy melts, CRC Press, London, 2015, pp. 129–168.

[5] J.D. Hunt, K.A. Jackson, Nucleation of solid in an undercooled liquid by cavitation, J. Appl. Phys. 37 (1966) 254–257, https://doi.org/10.1063/1.1707821.

[6] K. Yasui, Acoustic Cavitation and Bubble Dynamics, Springer International Publishing, Cham, 2018, https://doi.org/10.1007/978-3-319-68237-2.

[7] F. Wang, D. Eskin, J. Mi, T. Connolley, J. Lindsay, M. Mounib, A refining mechanism of primary Al3Ti intermetallic particles by ultrasonic treatment in the liquid state, Acta Mater. 116 (2016) 354–363, https://doi.org/10.1016/j.actamat.2016.06.056.

[8] F. Wang, D. Eskin, J. Mi, C. Wang, B. Koe, A. King, C. Reinhard, T. Connolley, A synchrotron X-radiography study of the fragmentation and refinement of primary intermetallic particles in an Al-35 Cu alloy induced by ultrasonic melt processing, Acta Mater. 141 (2017) 142–153, https://doi.org/10.1016/j.actamat.2017.09.010.

[9] J. Mi, D. Tan, T.L. Lee, In Situ Synchrotron x-ray study of ultrasound cavitation and its effect on solidification microstructures, Metall. Mater. Trans. B 46 (2015) 1615–1619, https://doi.org/10.1007/s11663-014-0256-z.

[10] W. Mirihanage, W. Xu, J. Tamayo-Ariztondo, D. Eskin, M. Garcia-Fernandez, P. Srirangam, P. Lee, Synchrotron radiographic studies of ultrasonic melt processing of metal matrix nano composites, Mater. Lett. 164 (2016) 484–487, https://doi.org/10.1016/j.matlet.2015.11.022.

[11] Z. Zhang, C. Wang, B. Koe, C.M. Schlepütz, S. Irvine, J. Mi, Synchrotron X-ray imaging and ultrafast tomography in situ study of the fragmentation and growth dynamics of dendritic microstructures in solidification under ultrasound, Acta Mater. 209 (2021), 116796, https://doi.org/10.1016/j.actamat.2021.116796.

[12] S. Wang, J. Kang, Z. Guo, T.L. Lee, X. Zhang, Q. Wang, C. Deng, J. Mi, In situ high speed imaging study and modelling of the fatigue fragmentation of dendritic structures in ultrasonic fields, Acta Mater. 165 (2019) 388–397, https://doi.org/10.1016/j.actamat.2018.11.053.

[13] B. Schneiderman, A.C. Chuang, P. Kenesei, Z. Yu, In situ synchrotron diffraction and modeling of non-equilibrium solidification of a MnFeCoNiCu alloy, Sci. Rep. 11 (2021) 5921, https://doi.org/10.1038/s41598-021-85430-z.

[14] T.V. Atamanenko, D.G. Eskin, L. Zhang, L. Katgerman, Criteria of grain refinement induced by ultrasonic melt treatment of aluminum alloys containing Zr and Ti, Metall. Mater. Trans. A 41 (2010) 2056–2066, https://doi.org/10.1007/s11661-010-0232-4.

[15] G. Wang, Q. Wang, M.A. Easton, M.S. Dargusch, M. Qian, D.G. Eskin, D.H. StJohn, Role of ultrasonic treatment, inoculation and solute in the grain refinement of commercial purity aluminium, Sci. Rep. 7 (2017) 9729, https://doi.org/10.1038/s41598-017-10354-6.

[16] B. Wang, D. Tan, T.L. Lee, J.C. Khong, F. Wang, D. Eskin, T. Connolley, K. Fezzaa, J. Mi, Ultrafast synchrotron X-ray imaging studies of microstructure fragmentation in solidification under ultrasound, Acta Mater. 144 (2018) 505–515, https://doi.org/10.1016/j.actamat.2017.10.067.

[17] M.H. Farshidianfar, A. Khajepour, A.P. Gerlich, Effect of real-time cooling rate on microstructure in laser additive manufacturing, J. Mater. Process. Technol. 231 (2016) 468–478, https://doi.org/10.1016/j.jmatprotec.2016.01.017.

[18] H.-H. König, N.H. Pettersson, A. Durga, S. Van Petegem, D. Grolimund, A. C. Chuang, Q. Guo, L. Chen, C. Oikonomou, F. Zhang, G. Lindwall, Solidification modes during additive manufacturing of steel revealed by high-speed X-ray diffraction, Acta Mater. 246 (2023), 118713, https://doi.org/10.1016/j.actamat.2023.118713.

[19] L.I. Escano, S.J. Clark, A.C. Chuang, J. Yuan, Q. Guo, M. Qu, W. Dong, X. Zhang, J. Huang, K. Fezzaa, P. Kenesei, B.J. Walker, T. Sun, K.W. Eliceiri, L. Chen, An electron beam melting system for in-situ synchrotron X-ray monitoring, Addit. Manuf. Lett. 3 (2022), 100094, https://doi.org/10.1016/j.addlet.2022.100094.

[20] T. Wang, V. Mazánová, X. Liu, Ultrasonic effects on gas tungsten arc based wire additive manufacturing of aluminum matrix nanocomposite, Mater. Des. 214 (2022), 110393, https://doi.org/10.1016/j.matdes.2022.110393.

[21] E. Chauvet, P. Kontis, E.A. Jägle, B. Gault, D. Raabe, C. Tassin, J.-J. Blandin, R. Dendievel, B. Vayre, S. Abed, G. Martin, Hot cracking mechanism affecting a non-weldable Ni-based superalloy produced by selective electron Beam Melting, Acta Mater. 142 (2018) 82–94, https://doi.org/10.1016/j.actamat.2017.09.047.

[22] N. Wang, S. Mokadem, M. Rappaz, W. Kurz, Solidification cracking of superalloy single- and bi-crystals, Acta Mater. 52 (2004) 3173–3182, https://doi.org/10.1016/j.actamat.2004.03.047.

[23] L. Zhou, S. Chen, M. Ma, Jing Liang, J. Chen, M. Wang, The dynamic recrystallization mechanism of ultrasonic power on non-contact ultrasonic-assisted direct laser deposited alloy steel, Mater. Sci. Eng.: A 840 (2022), 142971, https://doi.org/10.1016/j.msea.2022.142971.

[24] C.J. Todaro, M.A. Easton, D. Qiu, D. Zhang, M.J. Bermingham, E.W. Lui, M. Brandt, D.H. StJohn, M. Qian, Grain structure control during metal 3D printing by high-intensity ultrasound, Nat. Commun. 11 (2020) 142, https://doi.org/10.1038/s41467-019-13874-z.

[25] Z. Liu, X. Jin, J. Zhang, Z. Hao, J. Li, Microstructure evolution and mechanical properties of SUS301L stainless steel sheet welded joint in ultrasonic vibration assisted laser welding, Opt. Laser Technol. 153 (2022), 108193, https://doi.org/10.1016/j.optlastec.2022.108193.

[26] N. Allain-Bonasso, F. Wagner, S. Berbenni, D.P. Field, A study of the heterogeneity of plastic deformation in IF steel by EBSD, Mater. Sci. Eng.: A 548 (2012) 56–63, https://doi.org/10.1016/j.msea.2012.03.068.

[27] J.C. Lippold, Welding Metallurgy and Weldability, 1st ed., Wiley, 2015 https://doi.org/10.1002/9781118960332.

[28] X. Feng, F. Zhao, H. Jia, J. Zhou, Y. Li, W. Li, Y. Yang, Effect of temperature conditions on grain refinement of Mg–Al alloy under ultrasonic field, Int. J. Cast Met. Res. 30 (2017) 341–347, https://doi.org/10.1080/13640461.2017.1317392.

[29] S.-B. Kim, Y.-H. Cho, M.-S. Jo, J.-G. Jung, Y.-K. Lee, J.-M. Lee, Quantitative approach to realization of ultrasonic grain refinement of Al-7Si-2Cu-1Mg alloy, Sci. Rep. 9 (2019) 17812, https://doi.org/10.1038/s41598-019-54161-7.

[30] U. Shah, X. Liu, A. Benatar, A. Kuprienko, W. Zhang, Computational analysis of the ultrasonic effects on resistance spot welding process, J. Manuf. Process. 81 (2022) 191–201, https://doi.org/10.1016/j.jmapro.2022.06.050.